RSC Advances

ROYAL SOCIETY OF CHEMISTRY

www.rsc.org/advances

Graphical Abstract:

Cobalt sulfide nanoparticles impregnated nitrogen and sulfur co-doped graphene nanosheets synthesized in water-based media are found to be an inexpensive but efficient bifunctional catalyst that equips rechargeable Zn-air batteries with good cycling stability.

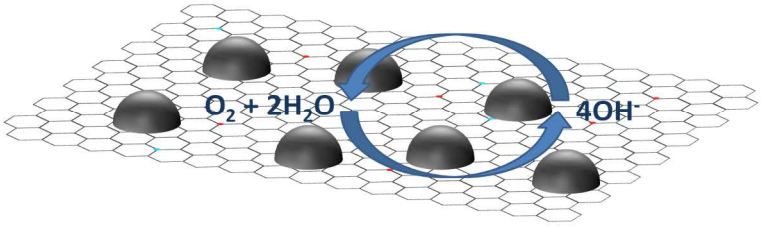

Journal Name

RSCPublishing

COMMUNICATION

Cobalt Sulfide Nanoparticles Impregnated Nitrogen and Sulfur co-Doped Graphene as Bifunctional Catalyst for Rechargeable Zn-air Batteries

Cite this: DOI: 10.1039/xoxxoooooox

Received ooth January 2012,
Accepted ooth January 2012

DOI: 10.1039/xoxxoooooox

www.rsc.org/

Dongsheng Geng,[a] Ni-Ni Ding,[a] T. S. Andy Hor,[*,a,b] Sheau Wei Chien,[a] Zhaolin Liu,[*,a] Yun Zong[*,a]

We report cobalt sulfide nanoparticles decorated nitrogen & sulfur co-doped graphene nanosheets as an effective bifunctional oxygen catalyst. Its oxygen evolution reaction (OER) catalytic activity outperforms Pt/C, giving a current density of 38.19 mA•cm^{-2} at 1.0 V. Zn-air batteries using this material on air-cathode show high stability and good rechargeability.

Ever-growing awareness in sustainable development has been a key drive for environmentally friendly electric vehicles (EVs). Zn-air rechargeable battery using aqueous electrolyte has emerged as a promising candidate thanks to their high specific energy density (1084 Wh·kg^{-1}), low cost and good safety[1,2] as compared to the prevailing lithium-ion batteries that offer a typical energy density of 200-250 Wh·kg^{-1} at relatively high cost with safety concerns. The commercialization viability of rechargeable Zn-air battery, however, is hindered by the issues of poor rechargeability, low power density and energy efficiency that associate with low columbic efficiency, sluggish oxygen reactions and high overpotential at the air-cathode of the batteries. A solution that helps circumvent such issues is an efficient bifunctional oxygen catalyst on air-cathode that facilitates oxygen reduction reaction (ORR) in discharge and oxygen evolution reaction (OER) in charge, respectively.[3,4]

Traditionally, bifunctional oxygen catalysts contain precious metals, such as Pt, Ru, Ir etc in high content which are far too costly. For applications using large battery packs, e.g. in electric vehicles, the bifunctional oxygen catalysts employed need to be inexpensive, environment-friendly and catalytically efficient.[5-7] Herein, we report such a catalyst prepared by integrating nitrogen and sulfur co-doped two-dimensional graphene nanosheets (GNs) of good ORR catalytic activity[8-10] with transition metal chalcogenide nanoparticles (NPs) of proven OER activity [11-15] via a facile one-pot hydrothermal reaction. This composite catalyst, N and S co-doped GNs decorated with CoS_x NPs, is found to be an effective bifunctional oxygen catalyst, giving good cycling stability in rechargeable Zn-air batteries.

Co-doping graphene with two different elements (particularly N and S) is a promising pathway to produce ORR catalyst, as it helps create non-neutral electron sites that enable efficient four-electron transfer ORR activity.[10] We use thiourea as the single precursor to react with graphene oxide (GO) to form N and S co-doped graphene nanosheets (NS-GNs), referring to a reported method[16,17]; however, the solvent in our reaction was changed from ethylene glycol (EG) to water and the reaction temperature was reduced from 200 ºC to 180 ºC. Despite a lower reaction temperature, the autogenic pressure inside the enclosed vessels for our water-based system is ~7 times higher than that of the EG-based system (10 *vs* 1.25 bar). As a consequence, instead of somewhat flat flakes, the resulted NS-GNs are heavily corrugated with interlinked nature of wrinkles as shown in the SEM (JEOL JSM-6700F) and TEM (Philips CM300-FEG instrument with operating voltage at 300 kV) images (Figure 1a & b), respectively. As thiourea reacts with GO in the presence of Co^{2+}, nucleation of Co_xS nanoparticles starts from surface of NS-GNs, the reductive co-doping product of graphene oxide, and these nuclei further grow into Co_xS nanoparticles of much larger sizes. A representative TEM image is shown in Figure 1c. One can see that spherical CoS_x nanoparticles with an average diameter of 50 nm are sitting on NS-GNs. The corrugation of the underlying NS-GNs in this case is not as serious as previously in the absence of Co^{2+}. A representative high resolution TEM (HR-TEM) image (Figure 1d) reveals that underneath the high crystalline Co_xS nanoparticles the NS-GNs are distorted with an average thickness of 7 layers. Such re-stacking of NS-GNs is likely caused by the high autogenic pressure of water at 180 ºC.

The co-existence of N and S on the surface of corrugated NS-GN flakes is evidenced by XPS (Thermo Scientific, Al K_α radiation) analysis (Figure 2a), which was introduced via the reaction of the hydrolysis products of thiourea, ammonia and hydrogen sulfide, with the oxygen-containing groups on GO under hydrothermal condition. The contents of elemental N and S are found to be 2.32 and 1.88 at%, respectively. The N1s spectrum is deconvoluted into two sets of signals (Figure 2b) which are attributed to the pyridinic-N (398.8 eV) and the quaternary-N (401.2 eV). The direct proof of the S doping in graphene is provided by the high resolution S2p spectrum in Figure 2c, which is resolved into 3 peaks at binding energies of 164.2, 165.7, and 168.5 eV, respectively. The first two match with the reported 2p3/2 and 2p1/2 positions of thiophene-S as a result of their spin-orbit coupling, while the 3rd one arises from the oxidized sulfur.[16,17] For CoS_x@NS-GNs, the XPS survey spectrum shows the

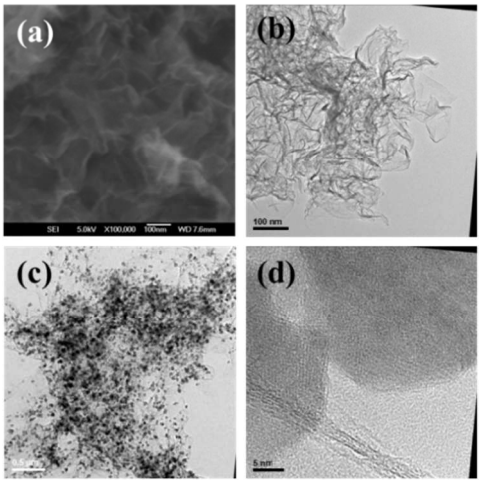

Figure 1 (a) A representative SEM image of N and S co-doped graphene nanosheets (NS-GNs), giving corrugated flake structure; (b) A representative TEM image of NS-GNs as ultrathin flexible flakes; (c) A representative TEM image of CoS_x@NS-GNs, where CoS_x nanoparticles are clearly visible on NS-GNs; (d) A representative HR-TEM image, indicating the existence of a few layers of NS-GNs in CoS_x@NS-GNs.

presence of C, N, S, O, and Co (Figure 2d). The ratio of Co to S is comfortably obtained from the EDS data (Figure 2e) as 2:3 (39.6:60.4) which seems to indicate a composition of Co_2S_3 for the obtained cobalt sulfide. Nevertheless, with the possible contribution of sulfur atoms on the surface of NS-GNs, this ratio of coincidental value should not be over-interpreted. In the as-prepared composite catalyst cobalt exists in a mixed valence state of Co(II) and Co(III), which will be further elaborated later.

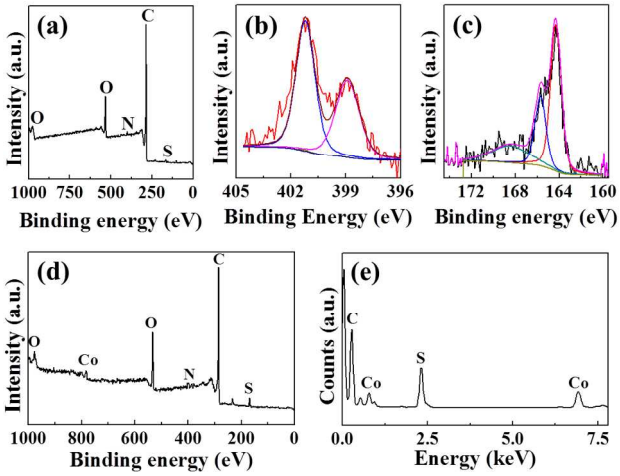

Figure 2 (a) XPS survey spectrum of NS-GNs; (b) High resolution N1s spectra of NS-GNs; (c) High resolution S2p spectra of NS-GNs; (d) XPS survey spectrum of CoS_x@NS-GNs; (e) EDS spectrum of CoS_x@NS-GNs.

The crystalline phase of obtained NS-GNs and Co_xS/NS-GNs are determined by XRD (Bruker D8 General Area Detector Diffraction System using Cu K_α radiation) measurement, and the diffraction data are shown in Figure 3a. One can see that the cobalt sulfide NPs grown on NS-GNs match the $Co_{1-x}S$ phase (ICDD PDF #00-042-0826) with hexagonal structure. As both CoS_x and $Co_{1-x}S$ are nonstoichiometric cobalt sulfides which are essentially interchangeable, for consistency reasons herein we will continue to use CoS_x@NS-GNs to denote the NS-GNs supported cobalt sulfides nanoparticles. The thermogravimetric analysis (TGA Q500, TA instruments) data of NS-GNs and CoS_x@NS-GNs are taken from room temperature to 900 ºC in air at a heating rate of 10 ºC min^{-1} to determine the content of CoS_x (Figure 3b). For NS-GNs (black line), the slow weight loss after 220 ºC is likely due to the removal of sulfur and nitrogen from the graphitic lattices, and the major weight loss at 550 to 675 ºC is attributed to the burn-off of graphitic carbons; whereas in CoS_x@NS-GNs (red line) similar major change takes place at 510 to 610 ºC, but with a much smaller weight loss. This may be due to the weight gain by a complicated oxidation of CoS_x which partially neutralizes the weight loss caused by the burn-off of graphitic carbons. The oxidized products of cobalt sulfide decompose further at temperature above 700 ºC to give stable cobalt oxides. Based on the TGA data the composition of CoS_x@NS-GNs is estimated to be about 63 wt% of NS-GNs and 37 wt% of CoS_x.

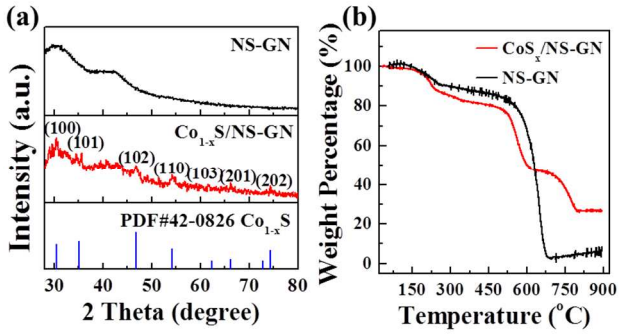

Figure 3 (a) XRD patterns of NS-GNs and CoS_x@NS-GNs, showing match of the cobalt sulfide with $Co_{1-x}S$; (b) TGA data of CoS_x@NS-GNs and NS-GNs in air from room temperature to 900 ºC that reveals the composition.

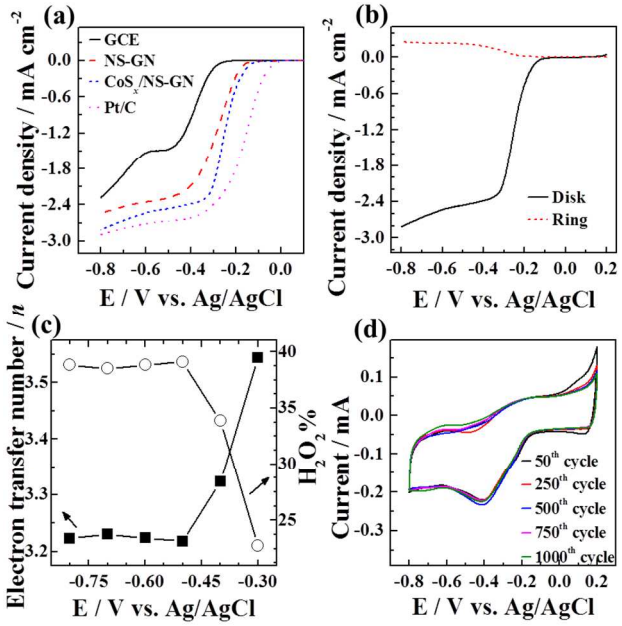

Figure 4 (a) Linear sweep voltammograms (LSVs) of GCE, NS-GNs, CoS_x@NS-GNs and Pt/C in O_2 saturated 0.1 M KOH aqueous solution at 1600 rpm with the sweep rate of 5 mV s^{-1}; (b) RRDE LSV of CoS_x@NS-GNs at a rotation rate of 1600 rpm; (c) The calculated number of electron transfer and H_2O_2% at varied potentials; (d) Cyclic voltammograms of CoS_x@NS-GNs in O_2-saturated 0.1 M KOH aqueous solution after 50, 250, 500, 750, 1000 cycles of scans, respectively. The potential sweep rate is 50 mV/s.

The ORR catalytic activity of CoS_x@NS-GNs was evaluated on an Autolab Potentiostat (PGSTAT302N, Metrohm) using rotating ring-disc electrode technique. Linear sweep voltammograms (LSVs) on glassy carbon electrode (GCE), NS-GNs, CoS_x@NS-GNs, and Pt/C were performed at a rotating rate of 1600 rpm and the results are presented together in Figure 4a. Unsurprisingly, typical LSV curve of non-noble metal ORR catalyst was observed for NS-GNs, which is in good agreement with reported results.[9,10,16] Herein, the onset electrode potential for the ORR (E_{ORR}) is defined as the potential at which the additional cathodic current is kept at 10 μA cm^{-2}. In this case, with decoration of CoS_x onto NS-GNs the resultant composite catalyst CoS_x@NS-GNs shows improvement in ORR onset potential by 27 mV (-0.147 *vs* -0.174 V), and ORR current by ~10% of increase. Nevertheless, its ORR activity is inferior to commercial Pt/C (-0.045 V) by a higher onset potential and a slightly lower ORR current (2.818 *vs* 2.900 mA) over the entire potential range. A summary of determinant parameters derived from Figure 4a is given below in Table 1. One can clearly see the improved ORR activity from NS-GNs to CoS_x@NS-GNs, which is likely attributed to a synergistic effect between CoS_x NPs and the NS-GNs support which was found in similar system previously.[18]

Table 1 Summary of the test data from half-cell (ORR and OER) and full cell (battery) using air-cathode of CoS_x@NS-GNs or Pt/C.

	ORR[a]		OER[b]		Zn-air battery		
Catal.	E_{ORR} (V)	j (mA cm^{-2})	E_{OER} (V)	j (mA cm^{-2})	E_{OCV} (V)	E_d[c] (V)	E_c[c] (V)
CoS_x@ NS-GN	-0.147	2.818	0.674	38.19	1.394	1.243	2.118
Pt/C	-0.045	2.900	0.657	27.52	1.451	1.211	2.129

[a] j at E=-0.8 V; [b] E at j = 3 mA cm^{-2} and j at 1.0 V. [c] E @ the 40th cycle. For the charging, the value was taken @ 50% of capacity.

The ORR catalytic mechanism of CoS_x@NS-GNs was further investigated to understand the selectivity of the ORR process, i.e. whether it undergoes a two-electron (forming HO_2^- intermediate) or a desirable four-electron process. The RRDE LSVs results are shown in Figure 4b, from which the number of electron transferred (n) and the percentage of H_2O_2 released (%H_2O_2) during ORR are calculated using the following equations:

$$\mathbf{n} = \frac{\mathbf{4I_d}}{\mathbf{I_d} + \frac{\mathbf{I_r}}{\mathbf{N}}} \qquad (1)$$

$$\%\mathbf{H_2O_2} = \frac{\mathbf{4 - n}}{\mathbf{2}} \times \mathbf{100}\% \qquad (2)$$

where I_d and I_r are the Faradic current on the disk and the ring, respectively, with N being the collection efficiency of the ring which was reported by the manufacture to be 0.37. From Figure 4b one can clearly see that I_r increases with the increase of I_d. Nevertheless, the current density on the ring electrode is notably smaller than that on the disk electrode, suggesting little hydrogen peroxide formation on the catalyst. The calculated number of electrons transferred during ORR is ~3.2 with the H_2O_2% being ~39% at the potentials lower than -0.5 V (Figure 4c). This seems to imply the involvement of two coexisting pathways, viz. two-electron and four-electron transfers (Equations 3 and 4), in the entire process with the latter being the dominant one.[19]

$$\mathbf{O_2 + H_2O + 2e^- \rightarrow HO_2^- + OH^-} \qquad (3)$$

$$\mathbf{O_2 + 2H_2O + 4e^- \rightarrow 4OH^-} \qquad (4)$$

A durability test on CoS_x@NS-GNs was carried out using cyclic voltammetry scans in O_2-saturated 0.1 M KOH aqueous solution. As shown in Figure 4d, little difference is visible after potential sweeps of 50, 250, 500, 750 and 1000 cycles, proving CoS_x@NS-GNs of excellent electrochemical stability under alkaline conditions which is important for the conventional rechargeable zinc-air battery used in this work.

To further understand the rechargeability, the OER activity (determining the charge behavior of metal-air batteries) of NS-GNs, CoS_x@NS-GN, and Pt/C were studied. The OER polarization curves measured in O_2-saturated 0.1 M KOH aqueous solution at 1600 rpm are shown in Figure 5. One can see that with the introduction of CoS_x onto NS-GNs the onset potential at the current density of 3 mA•cm^{-2} is lowered to 0.674 V, which is comparable to Pt/C (0.657 V). More interestingly, the OER specific activity of CoS_x@NS-GNs at 1.0 V is measured to be 38.19 mA•cm^{-2} which is 1.4 times as high as that of Pt/C (Table 1). The higher OER activity is likely attributed to the CoS_x nanoparticles, as NS-GNs are known poor for OER activity. The main function of NS-GNs here, apart from their ORR activity, is to provide a conductive network that facilitates efficient electron transfer. Nevertheless, some synergistic enhancement in the catalytic activity may arise from interaction of CoS_x nanoparticles with the underlying NS-GNs which is yet to be understood.[17,20]

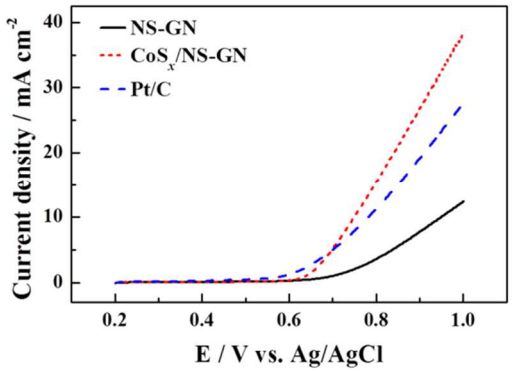

Figure 5 OER curves of NS-GN, CoS_x@NS-GN, and Pt/C in O_2 saturated 0.1 M KOH at 1600 rpm with the sweep rate of 5 mV s^{-1}. The current density on CoS_x@NS-GNs at 1.0 V is 38.19 mA•cm^{-2}, which is 1.4 times as high as that of Pt/C.

Zn-air batteries were built using CoS_x@NS-GNs or commercial Pt/C catalyst as air-cathode material to evaluate the rechargeability of the batteries in discharge-charge cycling experiments. The testing results are shown in Figure 6a and also summarized in Table 1. One can see that as CoS_x@NS-GNs were used as cathode material, the battery can be easily discharged and charged for 50 cycles at 1.25 mA•cm^{-2} over a period of 50 h with almost a constant discharge voltage of ~1.23 V. In contrast, Pt/C suffers a loss of 11% in the discharge voltage (1.35 → 1.20 V). In the charge processes, the charge voltage even sees a slight improvement for CoS_x@NS-GNs upon cycling; whereas Pt/C encounters a clear rise in the charge voltage. Such difference in the change of charge and discharge voltages between the both samples during the repetitive charge-discharge processes can be better viewed in Figure 6b, in which the average discharge and charge potentials for the consecutive 50 cycles are plotted. A close-up view of the discharge-charge curves in the 40th cycle of both cells is given in Figure 6c, whereby the above-

described difference is seen more clearly. It is also reflected by the larger difference between E_{OCV} and the discharge potential after 40 cycles of discharge-charge for Zn-air batteries using Pt/C based air-cathode (0.240 V) than that of its counterpart using the air-cathode of composite catalyst CoS_x@NS-GNs (0.151 V). With comparable catalytic performance to Pt/C, CoS_x@NS-GNs will provide potential inexpensive alternatives for rechargeable Zn-air batteries.[21,22]

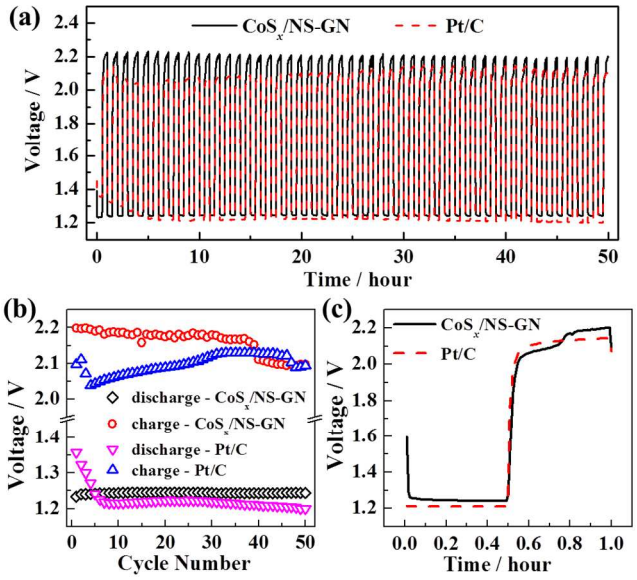

Figure 6. (a) Cycling performance of Zn-air battery at 1.25 mA•cm^{-2} and 1-hr per cycle over 50 h using CoS_x@NS-GN and Pt/C as catalyst, respectively. (b) The average discharge and charge potentials for the consecutive 50 cycles. (c) Typical discharge and charge polarization curves of CoS_x@NS-GN and Pt/C for the fortieth cycle, respectively.

Conclusion

In conclusion, we synthesized an inexpensive composite catalyst, CoS_x@NS-GNs, from a water-based reaction that shows comparable performance to Pt/C catalyst. Zinc-air rechargeable battery built using CoS_x@NS-GNs as air cathode material exhibits excellent cycling stability, proving feasibility and significance of integrating N/S co-doped graphene nanosheets with nanosized metal sulfides in the design of ORR and OER bifunctional catalysts. Such catalysts as sustainable electrode material are likely to take a more central stage in the current surge of interest in metal-air battery research.

Acknowledgement

This work was supported by the project IMRE/12-2P0504 under the SERC Advanced Energy Storage Research Programme, and Institute of Material Research and Engineering (IMRE), A*STAR, Singapore. The authors thank Dr. Zheng Zhang for his help with the XPS measurement.

Notes and references

[a] Institute of Materials Research and Engineering, A*STAR (Agency for Science, Technology and Research), 3 Research Link, Singapore 117602; E-mails: zl-liu@imre.a-star.edu.sg (Z Liu); y-zong@imre.a-star.edu.sg (Y Zong).
[b] Department of Chemistry, National University of Singapore, 3 Science Drive 3, Singapore 117543; E-mail: andyhor@nus.edu.sg.

1. J.-S. Lee, S. Tai Kim, R. Cao, N.-S. Choi, M. Liu, K. T. Lee, J. Cho, *Adv. Energy Mater.*, 2011, **1**, 34-50.
2. P. Sapkota, H. Kim, *J. Ind. Eng. Chem.*, 2009, **15**, 445-450.
3. J.-G. Zhang, P. G. Bruce, X. G. Zhang, in Handbook of Battery Materials, Wiley-VCH Verlag GmbH & Co. KGaA, 2011, pp. 757-795.
4. V. Neburchilov, H. Wang, J. J. Martin, W. Qu, *J. Power Sources*, 2010, **195**, 1271-1291.
5. F. Cheng, J. Chen, *Chem. Soc. Rev.*, 2012, **41**, 2172-2192.
6. R. Cao, J.-S. Lee, M. Liu, J. Cho, *Adv. Energy Mater.*, 2012, **2**, 816-829.
7. L. Jörissen, *J. Power Sources*, 2006, **155**, 23-32.
8. L. Dai, *Acc. Chem. Res.*, 2012, **46**, 31-42.
9. S. Yang, L. Zhi, K. Tang, X. Feng, J. Maier, K. Müllen, *Adv. Funct. Mater.*, 2012, **22**, 3634-3640.
10. J. Liang, Y. Jiao, M. Jaroniec, S. Z. Qiao, *Angew. Chem. Int. Ed.*, 2012, **51**, 11496-11500.
11. N. Alonso-Vante, in Electrocatalysis in Fuel Cells, Vol. 9 (Eds.: M. Shao), Springer London, 2013, pp. 417-436.
12. M.-R. Gao, J. Jiang, S.-H. Yu, *Small*, 2012, **8**, 13-27.
13. H. Wang, Y. Liang, Y. Li, H. Dai, *Angew. Chem. Int. Ed.*, 2011, **50**, 10969-10972.
14. N. Mahmood, C. Zhang, J. Jiang, F. Liu, Y. Hou, *Chem. Eur. J.*, 2013, **19**, 5183-5190.
15. N. M. Dimitrijevic, S. Li, M. Grätzel, *J. Am. Chem. Soc.*, 1984, **106**, 6565-6569.
16. Y. Su, Y. Zhang, X. Zhuang, S. Li, D. Wu, F. Zhang, X. Feng, *Carbon*, 2013, **62**, 296-301.
17. Q. Liu, J. Jin, J. Zhang, *ACS Appl. Mater. Interfaces*, 2013, **5**, 5002-5008.
18. Y. Liang, Y. Li, H. Wang, J. Zhou, J. Wang, T. Regier, H. Dai, *Nat. Mater.*, 2011, **10**, 780-786.
19. M. Seredych, J.-C. Idrobo, T. J. Bandosz, *J. Mater. Chem. A*, 2013, **1**, 7059-7067.
20. W. G. Hardin, D. A. Slanac, X. Wang, S. Dai, K. P. Johnston, K. J. Stevenson, *J. Phys. Chem. Lett.*, 2013, **4**, 1254-1259.
21. Z. Chen, A. Yu, D. Higgins, H. Li, H. Wang, Z. Chen, *Nano Lett.*, 2012, **12**, 1946-1952.
22. Y. Li, M. Gong, Y. Liang, J. Feng, J.-E. Kim, H. Wang, G. Hong, B. Zhang, H. Dai, *Nat. Commun.*, 2013, **4**, 1805.